Biomaterials and Biosystems 22 (2026) 100135

Contents lists available at ScienceDirect

Biomaterials and Biosystems

journal homepage: www.elsevier.com/locate/bbiosy

Electrochemical sensor based on MWCNTs/ZnONPs for detection of prostate specific antigen

Chiravoot Pechyen [a,b], Khanittha Ponsanti [c], Benchamaporn Tangnorawich [b,c], Surachet Toommee [d,*], Yardnapar Parcharoen [e,*]

[a] Department of Materials and Textile Technology, Faculty of Science and Technology, Thammasat University, Patumthani 12120, Thailand
[b] Thammasat University Center of Excellence in Modern Technology and Advanced Manufacturing for Medical Innovation, Thammasat University, Patumthani 12120, Thailand
[c] Department of Physics, Faculty of Science and Technology, Thammasat University, Patumthani 12120, Thailand
[d] Materials and Industrial Engineering Program, Faculty of Industrial Technology, Kamphaeng Phet Rajabhat University, Kamphaeng Phet, 62000, Thailand
[e] Chulabhorn International College of Medicine, Thammasat University, Patumthani 12120, Thailand

ARTICLE INFO

Keywords:
Multiwalled carbon nanotubes
ZnO nanoparticles
Electrochemical biosensor
Prostate-specific antigen

ABSTRACT

An electrochemical immunosensor based on multiwalled carbon nanotube/zinc oxide nanoparticle (MWCNTs/ZnONPs) composites was fabricated for the sensitive and selective detection of prostate-specific antigen (PSA), an established biomarker for early prostate cancer diagnosis. The MWCNTs/ZnONPs-modified screen-printed carbon electrode (SPCE) provided an enlarged electroactive surface area and enhanced electron transfer kinetics, thereby improving the overall analytical performance. Monoclonal anti-PSA antibodies were covalently immobilized on the composite surface and PSA quantification was conducted using cyclic voltammetry (CV) and differential pulse voltammetry (DPV). Under optimized experimental conditions, the biosensor exhibited a linear response toward PSA concentrations ranging from 5 to 200 ng mL^{-1}, with a detection limit of 5 ng mL^{-1} (R^2 = 0.979). The proposed platform demonstrated good sensitivity, specificity, and operational stability, whereas negligible interference was observed for potential coexisting species, such as glucose, bovine serum albumin (BSA), and ascorbic acid. Glucose showed minimal current variation because of its weak electroactivity under the selected conditions, while BSA produced only a slight signal increase, likely due to limited protein adsorption onto the electrode surface. In contrast, ascorbic acid generated a relatively higher current response owing to its intrinsic electrochemical activity; however, its electrochemical profile remained distinguishable from the PSA signal. The good anti-interference performance was attributed to the combined effect of the conductive MWCNTs/ZnONPs platform and the BSA blocking layer, which reduced non-specific adsorption while preserving efficient electron transfer. Because of its easy fabrication, cost-effectiveness, and reliable analytical performance, the MWCNT/ZnONP/SPCE immunosensor is promising as a portable point-of-care device for prostate cancer screening.

1. Introduction

Prostate cancer is a cancer found in men, typically those over the age of especially older men, and develops in the male reproductive system. It is often a latent cancer that exhibits no symptoms in its early stages. Prostate-specific antigen (PSA) is a 32–33 kDa serine protease secreted by the prostate gland into the seminal fluid and is widely accepted as a biomarker for this purpose [1,2]. In healthy individuals, serum PSA levels generally remain below 4 ng mL^{-1}; persistent elevation often suggests abnormal prostate activity or tumor development [3].

Conventional detection methods, including enzyme-linked immunosorbent assays (ELISA), high-performance liquid chromatography (HPLC), and mass spectrometry, are recognized for their precision, but are time-consuming, costly, and dependent on laboratory expertise [4,5]. In the past decade, various advanced PSA assays have been reported, including photoelectrochemical aptasensors based on exciton–plasmon interactions between AuNPs/graphene nanohybrids and CdS QDs/TiO_2 [6], and smartphone-based photoelectrochemical immunoassays using Co-doped Bi_2O_2S nanosheets as photoactive materials for portable PSA detection [7]. Electrochemical biosensors have recently gained attention

* Corresponding authors.
E-mail addresses: surachet_t@kpru.ac.th (S. Toommee), yardnapa@tu.ac.th (Y. Parcharoen).

https://doi.org/10.1016/j.bbiosy.2026.100135
Received 17 November 2025; Received in revised form 30 March 2026; Accepted 31 March 2026
Available online 31 March 2026

as practical alternatives because they provide rapid measurement, high sensitivity, and the possibility of portable point-of-care operation.

Recent work has shown that electrochemical immunoassays can be integrated with smartphones for point-of-care detection of viral proteins, such as the SARS-CoV-2 nucleocapsid protein [8], and that sophisticated photocurrent-polarity-switching strategies can be used to modulate signal readout by dynamically tuning the spatial distance of electroactive tags [9]. These examples highlight the engineering of electrochemical and photoelectrochemical formats for compact, user-friendly diagnostic devices.

Among the various nanomaterials used for electrode modification, multiwalled carbon nanotubes (MWCNTs) are notable for their large surface area, strong electrical conductivity, and mechanical durability [10,11]. Zinc oxide nanoparticles (ZnONPs) complement these properties with good biocompatibility and high isoelectric point, which favors antibody attachment [12–14]. When combined, MWCNTs and ZnONPs form a synergistic hybrid that enhances electron transfer and improves signal stability.

In parallel, significant efforts have been devoted to translating nanostructured platforms into robust point-of-care (POC) formats. For instance, $NaNbO_3$ semiconductors have been exploited by combining their photoelectric and piezoelectric properties for POC immunoassays [15], and paper electrode-based flexible pressure sensors have been developed for POC immunoassays that can be read with a simple digital multimeter [16]. Although different electrochemical immunosensors for PSA have been reported, many rely on complex nanostructures, multiple labeling steps, photoelectrochemical illumination setups, or custom-made electrodes, which can increase the fabrication cost and complicate the translation into routine POC testing [17–25].

This study demonstrates that rationally engineered transducer materials can be integrated with low-cost substrates to develop disposable and portable sensing platforms suitable for near-patient use. Multiwalled carbon nanotube/zinc oxide nanoparticle (MWCNTs/ZnONPs) composites were synthesized using an eco-friendly guava-extract-assisted method. The composite offers several advantages: MWCNTs supply a highly conductive sp^2 network and large electroactive surface area for efficient charge transfer, whereas ZnONPs provide a high isoelectric point and abundant surface hydroxyl groups that facilitate antibody immobilization. In contrast, the major motivation of the present work is not to introduce a new sensing mechanism but to demonstrate that a simple, label-free, one-step voltammetric immunosensor can be constructed by integrating green-synthesized ZnO nanoparticles with multiwalled carbon nanotubes on a disposable screen-printed carbon electrode (Fig. 1).

2. Materials and methods

2.1. Materials

Multiwalled carbon nanotubes MWCNTs (>98% carbon basis, O.D. × *L* 6–13 nm × 2.5–20 μm; CAS No 308,068-56–6), and zinc nitrate hexahydrate ($Zn(NO_3)_2{\cdot}6H_2O$, 99%; CAS No 10,196-18–6) were purchased from Sigma-Aldrich (Bangkok, Thailand). Fresh guava fruit (*Psidium guajava L.*) was obtained from a local market in Bangkok, Thailand. Phosphate buffer solution (PBS, 0.1 M, pH 7.4; CAS No 7558–79–4 for Na_2HPO_4 / CAS No 7778–77–0 for KH_2PO_4), potassium chloride (KCl; CAS No 7447–40–7), potassium ferrocyanide trihydrate ($K_4[Fe(CN)_6]{\cdot}3H_2O$; CAS No 14,459-95–1), potassium ferricyanide ($K_3[Fe(CN)_6]$; CAS No 13,746-66–2), and ethanol (absolute; CAS No 64–17–5) were purchased from Sigma-Aldrich, Bangkok, Thailand.

Screen-printed carbon electrodes (SPCEs) were supplied by Quasense Co. Ltd. (Bangkok, Thailand). 1-Ethyl-3-(3-dimethylaminopropyl) carbodiimide hydrochloride (EDC; CAS No 25,952-53–8), N-hydroxysuccinimide (NHS; 98%; CAS No 6066–82–6), mouse monoclonal anti-KLK3 antibody (anti-PSA; CAS No N/A), recombinant human PSA (CAS No 117,716-79–3), ascorbic acid (CAS 50–81–7), glucose (CAS 50–99–7), and bovine serum albumin (BSA, CAS: 9048-46-8) were purchased from Sigma-Aldrich, Bangkok, Thailand.

All chemicals were of analytical or research grade and were used as received. Ultrapure water (18.2 MΩ·cm) was obtained using a Milli-Q purification system (Millipore, Bedford, MA, USA).

2.2. Preparation of ZnO nanoparticles (ZnONPs)

ZnO nanoparticles (ZnONPs) were synthesized using a green synthesis method with guava peel extract as the reducing and stabilizing agent. In a typical procedure, 4 g of zinc nitrate hexahydrate ($Zn(NO_3)_2{\cdot}6H_2O$) was added to freshly prepared guava peel extract and stirred continuously for 60 min at room temperature. The mixture was heated in a water bath at 60 °C for 1 h, followed by centrifugation at 5000 rpm for 30 min. The solid product was collected, dried at 150 °C, and calcined in a furnace at 400 °C for 1 h to yield ZnO nanoparticles.

2.3. Preparation of MWCNTs/ZnONPs/antibody-PSA electrodes

For the preparation of MWCNTs/ZnONPs composites, 10 mg of multiwalled carbon nanotubes (MWCNTs) was dispersed in 10 mL of ethanol by ultrasonication for 30 min. Then, 10 mg of ZnO NPs was added, and the suspension was sonicated for a further 30 h to obtain a uniform dispersion.

A 2.5 μL aliquot of the prepared MWCNTs/ZnONPs composite was drop-cast onto a screen-printed carbon electrode (SPCE) and air-dried to

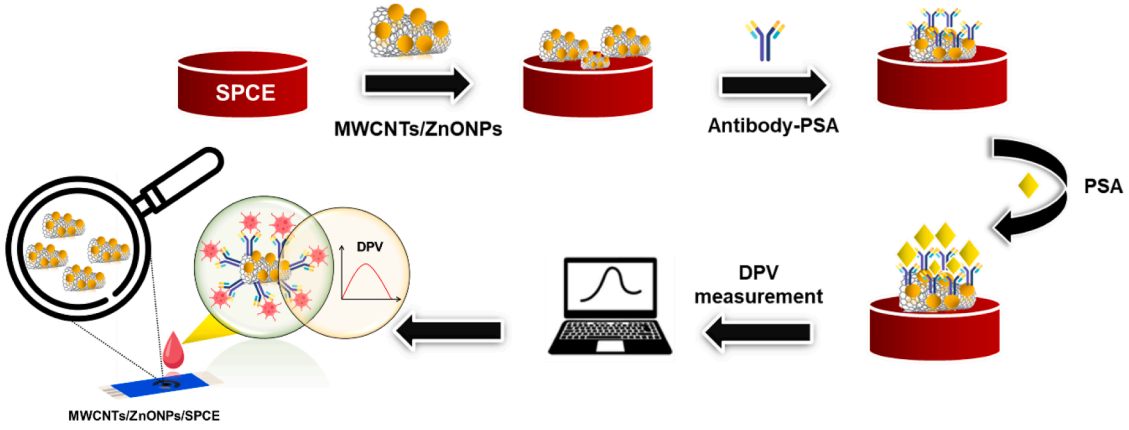

Fig. 1. Schematic depicting the electrochemical sensing of PSA using MWCNTs/ZnONPs/antibody-PSA electrodes.

remove the solvent, yielding the modified electrode (MWCNTs/ZnONPs/SPCE). The electrode surface was activated using a mixture of 1-ethyl-3-(3-dimethylaminopropyl) carbodiimide (EDC; 0.2 M) and N-hydroxysuccinimide (NHS; 0.05 M) in PBS and stirred at room temperature for 12 h.

After activation, 1 μL of the anti-PSA antibody solution was added to the modified electrode surface and incubated at 4 °C overnight for antibody immobilization. The resulting MWCNTs/ZnONPs/anti-PSA electrodes were stored at 4 °C until further use. The same procedure was repeated for the composites with different MWCNTs: ZnONPs mass ratios (1:1, 1:2, and 2:1).

2.4. Characterization of MWCNTs/ZnONPs

The structural properties of the MWCNTs and MWCNTs/ZnONPs were analyzed using powder X-ray diffraction (PXRD) with a Bruker D8 Discover diffractometer (Bruker AXS GmbH, Karlsruhe, Germany) equipped with Cu Kα radiation (λ = 1.5406 Å) operated at 40 kV and 40 mA. The morphology was examined using scanning electron microscopy (SEM; HITACHI IT500HR, Tokyo, Japan). The elemental composition was verified by energy-dispersive X-ray spectroscopy (EDS/EDX; Oxford Instruments, Abingdon, UK) at 20 kV.

Dynamic light scattering (DLS) analysis was performed to determine the particle size distribution using a HORIBA SZ-100 nanoparticle analyzer (Kyoto, Japan) at 25 °C and a 90° scattering angle. Raman spectra were recorded with a DXR3 Raman Microscope (Thermo Fisher Scientific, Waltham, MA, USA) using a 532 nm Ar laser excitation source.

Electrochemical measurements were performed on a PalmSens4 electrochemical workstation (PalmSens BV, Houten, Netherlands) using the PS-39E8 software package. A conventional three-electrode configuration was employed, consisting of an Ag/AgCl reference electrode, platinum counter electrode, and modified MWCNTs/ZnONPs/SPCE working electrode. Cyclic voltammetry (CV) and differential pulse voltammetry (DPV) were performed for analytical evaluation.

2.5. In vitro biological interference study

All measurements were performed in 0.1 M phosphate-buffered saline (PBS, pH 7.4) containing potassium ferricyanide $[Fe(CN)_6]^{3-/4-}$ as the redox probe and base line. The concentrations of interferents were selected to approximate physiological or clinically relevant levels: ascorbic acid at 0.1 mM, glucose at 5.0 mM, and BSA at 1.0 mg mL^{-1}. Cyclic voltammetry (CV) measurements were carried out at scan rate 0.1 V/s. The current responses obtained in the presence of each interferent were compared with the baseline. The changes in oxidation peak current were used to assess the degree of interference introduced by each biomolecule.

2.6. Protocol for detection of prostate specific antigen (PSA)

Electrochemical measurements were performed in PBS (pH 7.4) to maintain antibody stability under near-physiological conditions. All incubations were performed at room temperature (25 °C) to prevent antibody denaturation and ensure reproducibility. An incubation time of 30 min was selected, as this duration is sufficient to achieve antigen–antibody binding equilibrium in label-free electrochemical immunosensors.

For PSA detection, 10 μL of PSA solution prepared in PBS (pH 7.4) was drop-cast onto the MWCNTs/ZnONPs/anti-PSA–modified electrode surface and incubated under the conditions described above. After incubation, electrochemical measurements were performed using differential pulse voltammetry (DPV) with a PalmSens4 analyzer (PalmSens BV, Houten, Netherlands). The DPV parameters were set as follows: equilibration time = 0 s, initial potential (E_begin) = −0.1 V, final potential (E_end) = 0.5 V, potential step (E_step) = 0.005 V, pulse amplitude (E_pulse) = 0.05 V, pulse time (t_pulse) = 0.05 s, and scan rate = 0.05 V s^{-1}.

3. Results

3.1. Morphology particle size analysis and energy-dispersive X-ray spectroscopy (EDS) and Raman spectroscopy of MWCNTs/ZnONPs

SEM analysis (Figure S1A-2C) clearly shows the tubular morphology of MWCNTs, quasi-spherical ZnONPs, and uniform decoration of ZnONPs along the MWCNT framework. The images confirmed the roughened composite surface, which increased the available electroactive area for antibody attachment. The homogeneous distribution of ZnONPs on the carbon nanotube backbone indicates successful composite formation.

The EDS spectra confirmed the presence of C, Zn, and O in the MWCNTs/ZnONPs composites. Increasing the ZnONPs content resulted in higher Zn atomic percentages, verifying successful nanoparticle loading and tunable composite composition. No impurity elements were detected, indicating good material purity and effective integration of ZnONPs within the MWCNT matrix.

3.2. Raman spectroscopy and X-ray diffraction (XRD) analysis

The Raman spectra of MWCNTs and MWCNTs/ZnONPs composites are shown in Figure S1D. All samples exhibit the characteristic D band (~1357 cm^{-1}), G band (~1600 cm^{-1}), and G′ band (~2700 cm^{-1}), which are typical features of multiwalled carbon nanotubes. Upon incorporation of ZnONPs, a slight shift of the G band toward higher wavenumbers was observed. In addition, the intensity ratio of the D band to the G band (ID/IG) decreases from 1.07 for MWCNTs to 0.88–0.97 for the MWCNTs/ZnONPs composites.

The X-ray diffraction (XRD) patterns of MWCNTs and MWCNTs/ZnONPs composites are presented in Figure S1E. The diffraction peaks observed at 2θ = 25.53° and 42.86° correspond to the (002) and (100) planes of graphitic carbon, respectively, confirming the crystalline structure of the MWCNTs. Following the incorporation of ZnO nanoparticles, additional diffraction peaks were detected at 31.74°, 34.39°, 36.23°, 47.54°, 56.60°, 62.85°, 66.40°, 67.96°, and 69.09°, which are characteristic of the hexagonal wurtzite phase of ZnO, indicating the presence of crystalline ZnO within the composite materials. The main diffraction peaks used for crystallite size calculation were identified at 26.025° for MWCNTs and in the range of 36.120°–36.166° for the composite samples (Table S1). The full width at half maximum (FWHM) values were determined and applied to the Scherrer equation to estimate crystallite size. The MWCNTs exhibited a broader diffraction peak compared to the composite samples, while the MWCNTs/ZnONPs composites showed sharper and more defined peaks in the XRD patterns. The percentage crystallinity was determined from the ratio of crystalline area to total diffraction area for each sample.

3.3. Electrochemical characterization

The electrochemical behavior of the bare screen-printed carbon electrode (SPCE) and MWCNTs/ZnONPs-modified SPCE electrodes was investigated using cyclic voltammetry (CV) and electrochemical impedance spectroscopy (EIS), as shown in Figure S2. The CV curves recorded in 5 mM $K_3Fe(CN)_6$ containing 5 mM KCl (PBS, pH 7.4; scan rate 0.1 V s^{-1}) are presented in Figure S2 (CV Curve). Compared with the bare SPCE, all MWCNTs/ZnONPs-modified electrodes exhibited enhanced anodic and cathodic peak currents. Among the modified electrodes, the MWCNTs/ZnONPs/SPCE with a 1:2 mass ratio showed the highest redox peak current response, followed by the 2:1 and 1:1 ratios.

The EIS Nyquist plots of the bare and modified electrodes are shown in Figure S2 (EIS Nyquist plots). The bare SPCE exhibits a large semi-

circle diameter corresponding to a high charge-transfer resistance ($R_{ct} \approx 70\,k\Omega$). In contrast, the MWCNTs/ZnONPs-modified electrodes display significantly smaller semicircles, with the lowest R_{ct} value (≈10 kΩ) observed for the 1:2 composite.

3.4. In vitro biological interference study

Table S2 Approximate current changes induced by common biological interferents relative to baseline. Compared with the baseline, glucose produced almost no change in the oxidation current, showing only a slight decrease of −0.1 ± 0.05 μA. Bovine serum albumin caused only a modest increase in current of approximately 1.0 ± 0.2 μA. In contrast, ascorbic acid generated a more noticeable increase in anodic current of approximately 3.5 ± 0.5 μA, particularly in the positive potential region. Overall, the interferents caused only minor changes in the electrochemical response of the sensor platform. The magnitude of current variation followed the order: ascorbic acid > bovine serum albumin > glucose.

3.5. Electrochemical detection of prostate specific antigen

Differential pulse voltammetry (DPV) was used to evaluate the analytical performance of the MWCNTs/ZnONPs/SPCE/anti-PSA immunosensor for prostate-specific antigen (PSA) detection. The DPV responses recorded at different PSA concentrations are shown in Fig. 2A. A well-defined oxidation peak is observed at approximately 0.35 V, and the peak current increases progressively with increasing PSA concentration from 5 to 200 ng mL^{-1}.

The corresponding calibration plot of the peak current versus PSA concentration is presented in Fig. 2B Each data point represents the mean ± SD of three independent measurements ($n = 3$). A linear relationship was obtained over the concentration range of 5–200 ng mL^{-1}, described by the regression equation:

$$I_p(\mu A) = 0.2815C + 38.95$$

and correlation coefficient of $R^2 = 0.9824$. The limit of detection (LOD), calculated based on a signal-to-noise ratio of 3 using the standard deviation of blank measurements ($n = 3$), was 5 ng mL^{-1}.

The selectivity of the immunosensor was evaluated by comparing the DPV responses toward PSA with those obtained for potential interfering species, including albumin and ascorbic acid (AA), as shown in Fig. 2C-F. The responses from nonspecific biomolecules were negligible compared to that of PSA, indicating good selectivity of the sensor.

At this stage of the study, validation using real biological samples, such as human serum or plasma, was not conducted. Therefore, the results presented here reflect the intrinsic electrochemical sensing performance of the MWCNTs/ZnONPs-based platform under controlled experimental conditions.

4. Discussion

4.1. Morphology particle size analysis and energy-dispersive X-ray spectroscopy (EDS) and Raman spectroscopy of MWCNTs/ZnONPs

MWCNTs/ZnONPs composites were successfully synthesized using a green route, with guava extract acting as a reducing and stabilizing agent [17]. SEM micrographs (Figure S1) revealed well-dispersed ZnO nanoparticles deposited along the tubular structure of the MWCNTs. The

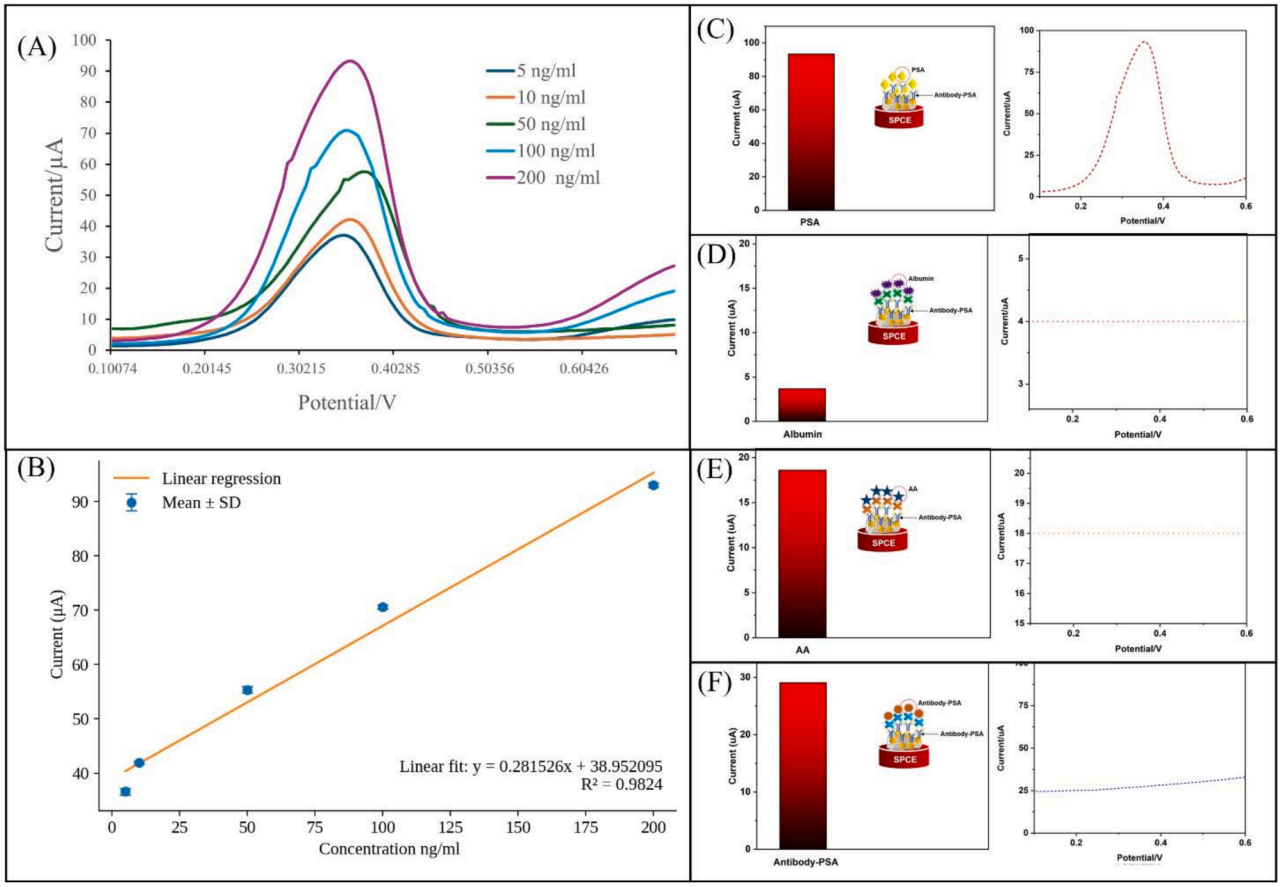

Fig. 2. (A) Differential pulse voltammetry (DPV) responses of the MWCNTs/ZnONPs/SPCE/anti-PSA electrode toward different PSA concentrations, and (B) corresponding calibration plot. Data are presented as the mean ± SD ($n = 3$ independent measurements). (C)-(F) Evaluation of the MWCNTs/ZnONPs/SPCE/antibody-PSA electrode against PSA, albumin, AA and antibody-PSA. Data are expressed as mean ± SD ($n = 3$).

ZnO NPs exhibited a roughly spherical morphology with an average diameter of approximately 60 nm. Such uniform decoration enhances the effective surface area and provides abundant active sites for biomolecule immobilization.

Dynamic light scattering (DLS) analysis confirmed particle size distributions of 49.9 μm, 48.23 μm, and 40 μm for the MWCNTs:ZnONPs ratios of 1:1, 2:1, and 1:2, respectively. The reduction in particle size with increasing ZnONPs content may contribute to an improved electrochemical response due to enhanced interfacial contact and a higher surface-to-volume ratio [18]. Similar morphologies have been reported for other MWCNTs–metal oxide hybrids used in biosensing applications [19].

The EDS spectra exhibited dominant signals corresponding to carbon (C), zinc (Zn), and oxygen (O), confirming the successful formation of the MWCNT–ZnO hybrid structure. The strong carbon signal originates from the multi-walled carbon nanotube backbone, whereas the zinc and oxygen peaks are characteristic of the ZnO nanoparticles anchored on the nanotube surface.

A clear compositional trend was observed with varying mass ratios of MWCNTs to ZnONPs. As the proportion of ZnONPs increased from 1:1 to 1:2 (MWCNTs:ZnONPs), the atomic percentage of Zn increased accordingly, while the relative carbon content decreased. This trend provides direct evidence for controlled ZnO loading and indicates that the nanoparticle deposition process is reproducible and composition-dependent [20]. Importantly, the oxygen-to-zinc atomic ratio remained close to the stoichiometric value expected for ZnO, suggesting that the nanoparticles maintained their oxide structure during composite formation.

4.2. Raman spectroscopy and X-ray diffraction (XRD) analysis

The Raman results indicate that the fundamental graphitic structure of the MWCNTs is preserved after ZnONPs modification. The D band reflects disordered carbon domains, whereas the G band is associated with the in-plane vibrations of sp^2-hybridized carbon atoms. The observed upshift of the G band after ZnONPs incorporation suggests interfacial charge transfer between the ZnO nanoparticles and the MWCNT framework, indicating strong electronic interactions within the hybrid composite. Furthermore, the reduction in the ID/IG ratio implies improved structural ordering and enhanced electronic coupling between the two components [21–23]. Improved crystallinity and interfacial charge transfer are critical factors for enhancing the electrochemical sensitivity of the resulting biosensor [24].

XRD analysis confirmed the successful incorporation of crystalline ZnO nanoparticles into the MWCNT framework. The preservation of the characteristic diffraction peaks of graphitic carbon indicates that the intrinsic crystalline structure of the MWCNTs remained intact after composite formation. The appearance of additional diffraction peaks corresponding to the hexagonal wurtzite phase of ZnO further demonstrates the formation of a hybrid composite rather than simple physical mixing or phase separation. The absence of impurity-related diffraction peaks suggests high phase purity of the synthesized materials, while the relatively sharp ZnO diffraction peaks indicate good crystallinity and strong interfacial interactions between the ZnO nanoparticles and the MWCNT network.

In addition to qualitative observations, quantitative analysis was performed using the Scherrer equation to estimate crystallite size and percentage crystallinity. The MWCNTs exhibited a relatively small crystallite size of 3.397 nm and low crystallinity (26.270%), whereas the MWCNTs/ZnONPs composites showed significantly larger crystallite sizes in the range of 13.297–13.441 nm and higher crystallinity values of 37.320–43.698%. This increase is consistent with the presence of highly crystalline ZnO domains within the composite structure, which contribute to sharper and more intense diffraction peaks [25].

The enhancement in crystallite size and crystallinity after ZnONPs incorporation suggests improved structural ordering and more defined crystalline domains in the composite system. The narrowing of diffraction peaks observed in the composite samples is in agreement with the inverse relationship between peak broadening and crystallite size described by the Scherrer equation. Similar trends have been reported in ZnO-based nanocomposites, where the introduction of ZnO nanoparticles leads to increased crystallinity and improved structural organization of the hybrid material [26].

Among the studied compositions, the MWCNTs/ZnONPs (2:1) sample exhibited the highest crystallinity (43.698%), indicating that this ratio may provide a more favorable balance between nanotube support and nanoparticle dispersion. This improved structural ordering is particularly beneficial for electrochemical applications, as higher crystallinity is often associated with enhanced electron transport and stability.

4.3. Electrochemical characterization

The enhanced redox responses observed for the MWCNTs/ZnONPs-modified electrodes can be attributed to the improved electron-transfer efficiency provided by the hybrid nanocomposite layer. The MWCNT framework offers continuous conductive pathways, whereas ZnONPs introduce additional electroactive sites, collectively facilitating rapid charge transport at the electrode–electrolyte interface [27,28].

The electrochemical performance of the MWCNTs/ZnONPs (1:2) electrode, as reflected by both the highest CV peak currents and the lowest charge-transfer resistance, indicates an optimal balance between ZnONPs loading and electrical conductivity. Excessive ZnO NPs may impede conductivity, whereas insufficient ZnO NPs reduce the number of active sites; the 1:2 ratio provides a favorable compromise that enhances interfacial electron transfer [29].

The electroactive surface area (A) of each electrode was estimated using the Randles–Sevcik equation [30]:

$$I_p = \left(2.69 \times 10^5\right) n^{3/2} A D^{1/2} \nu^{1/2} C \quad (1)$$

where $I_p$is the peak current (A), $n$is the number of electrons transferred, $A$is the electroactive surface area (cm^2), $D$is the diffusion coefficient ($cm^2\ s^{-1}$), $\nu$is the scan rate ($V\ s^{-1}$), and $C$is the bulk concentration of the redox probe ($mol\ cm^{-3}$).

Based on Eq. (1), the calculated electroactive surface areas were 0.3546 cm^2 for the bare SPCE and 0.1113 cm^2, 0.1613 cm^2, and 0.1142 cm^2 for the MWCNTs/ZnONPs/SPCE electrodes with mass ratios of 1:1, 2:1, and 1:2, respectively (Figure S3).

Although the calculated electroactive surface areas of the modified electrodes are lower than that of the bare SPCE, the substantial reduction in R_{ct}suggests that electrochemical performance is governed primarily by improved charge-transfer kinetics rather than geometric surface area alone. Moreover, the porous structure of the MWCNTs/ZnONPs composite provides abundant sites for antibody immobilization and facilitates efficient mass transport during antigen recognition.

The EIS results further confirm that the ZnONPs/MWCNTs hybrid network acts as an efficient electron mediator, consistent with previous reports on ZnO–carbon nanocomposites for electrochemical biosensing applications [31,32]. These findings support the selection of the MWCNTs/ZnONPs (1:2) composite as the optimal platform for subsequent immunosensor construction.

4.4. In vitro biological interference study

The minimal response observed for glucose is expected because glucose is only weakly electroactive under the selected electrochemical conditions and therefore does not significantly contribute to the measured current. Similarly, bovine serum albumin does not readily undergo direct redox reactions, and its slight current increase may be attributed to weak adsorption of protein molecules onto the electrode surface. In addition, BSA is widely used as a blocking agent in biosensors

because it can effectively reduce non-specific adsorption by occupying unreacted surface sites. Previous studies have shown that BSA blocking layers can prevent 68–100% of non-specific protein adsorption depending on the surface properties [33]. Ascorbic acid exhibited a larger signal change due to its intrinsic electrochemical activity and its ability to undergo oxidation at the electrode surface. However, despite the increased current, its electrochemical profile remained distinct from the expected PSA-induced response. The good anti-interference performance observed in this study is therefore likely due to the combined effect of the conductive MWCNTs/ZnONPs platform and the BSA blocking layer, which minimizes non-specific adsorption while maintaining electron transfer efficiency [34].

4.5. Electrochemical detection of prostate specific antigen

The gradual increase in the DPV peak current with increasing PSA concentration confirms successful antigen–antibody recognition at the electrode surface. The linear response observed over the clinically relevant range of 5–200 ng mL^{-1} demonstrated that the constructed immunosensor is suitable for PSA screening and follow-up monitoring applications. The obtained detection limit of 5 ng mL^{-1} is close to the commonly used clinical threshold for PSA-based prostate cancer screening, supporting its potential applicability in routine testing scenarios [35].

The high selectivity observed toward PSA can be attributed to the specific binding between immobilized anti-PSA antibodies and the target antigen, while the nonspecific adsorption of interfering biomolecules is effectively suppressed. This behavior is further supported by the stable electrochemical background provided by the MWCNTs/ZnONPs-modified electrode.

The enhanced sensing performance is primarily derived from the synergistic effects of the MWCNTs/ZnONPs nanocomposite. MWCNTs provide a highly conductive network and large surface area, facilitating rapid electron transport, whereas ZnONPs contribute abundant surface hydroxyl groups and oxygen vacancies that promote efficient antibody immobilization and bio-recognition events. The formation of a heterojunction between the sp^2-hybridized carbon nanotube framework and the ZnO semiconductor enhances interfacial charge transfer and reduces electron recombination during the redox process.

Similar cooperative charge-transfer mechanisms have been reported for hybrid biosensing platforms combining carbon nanomaterials with metal oxides or upconversion nanostructures for electrochemical and photoelectrochemical sensing applications [36–38]. The use of green-synthesized ZnO NPs further offers an environmentally benign alternative to conventional chemical synthesis routes, aligning with recent trends toward sustainable sensor fabrication [17,36,39].

Although the present immunosensor demonstrated good sensitivity, selectivity, and linearity within the clinically relevant PSA range, the detection limit remained close to the diagnostic cut-off value. Therefore, the current platform is more suitable for screening and monitoring purposes than the ultra-low-level PSA detection required for certain post-treatment evaluations. A comparison of the analytical performance of the proposed immunosensor with that of previously reported PSA electrochemical sensors is summarized in Table 1. Although several reported PSA sensors achieve lower limits of detection through complex nanostructures or multi-step amplification strategies, these systems often require sophisticated fabrication, labeling steps, or bulky instrumentation. In contrast, the proposed MWCNTs/ZnONPs/SPCE platform offers a simple fabrication process, compatibility with disposable electrodes, and straightforward electrochemical readout, making it attractive for low-cost and point-of-care applications.

For practical applications, further validation using real clinical samples is necessary. This may include recovery studies in spiked human serum and comparative analysis with established clinical methods, such as enzyme-linked immunosorbent assays (ELISA), followed by correlation and agreement analyses. The simple fabrication process and compatibility with disposable SPCEs suggest that the proposed MWCNTs/ZnONPs-based immunosensor has strong potential for integration into low-cost, point-of-care diagnostic devices, consistent with recent developments in portable electrochemical immunoassay platforms [16,42].

Table 1
Comparison of the analytical performance of representative electrochemical PSA biosensors reported in the literature and the present work.

Nanomaterials / Platform	Detection technique	LOD	Electrode type	References
rGO/AuNP/anti-PSA	SWV	3.0 pg mL^{-1}	GCE	[36]
Cu-MOF nanowire arrays/anti-PSA	SWV	0.6 pg mL^{-1}	Cu foam	[37]
Au/Fe-MOF nanocomposite immunosensor	Amperometry	0.9 pg mL^{-1}	GCE	[38]
Graphene nanocomposite aptasensor	DPV	1.2 pg mL^{-1}	GCE	[39]
CNT-reinforced bifunctional nanoplatform	DPV	2.0 pg mL^{-1}	GCE	[40]
Smartphone-based PEC with Co-doped Bi_2O_2S nanosheet	PEC	71.2 pg·mL^{-1}	SPCE	[7]
Flexible photosensitive pressure sensor + DMM immunoassay	POC / Pressure	12.6 pg mL^{-1}	Pressure-sensor	[41]
MWCNTs/ZnONPs/ anti-PSA	**DPV**	**5 ng mL^{-1}**	**SPCE/ MWCNTs/ ZnONPs**	**This work**

In addition, the achieved limit of detection is close to the commonly used clinical PSA cut-off value, which may restrict the applicability of the sensor for ultralow PSA monitoring in post-treatment or early relapse scenarios. Although the sensor demonstrated good reproducibility and acceptable short-term storage stability under controlled conditions. To further strengthen the biological relevance of the proposed sensor, future studies will focus on validation in complex biological matrices and clinical samples, as well as benchmarking against established diagnostic techniques.

5. Conclusion

This study presents the successful fabrication of an electrochemical biosensor that integrates multi-walled carbon nanotubes with zinc oxide nanoparticles on a screen-printed carbon electrode. The nanocomposite design greatly enhanced the surface area and charge-transfer efficiency, as confirmed by cyclic voltammetry and impedance studies. The optimized MWCNTs/ZnONPs (1:2) configuration exhibited a substantial reduction in charge-transfer resistance—from 70 kΩ for bare SPCE to approximately 10 kΩ—reflecting improved conductivity and interfacial activity. These structural and electrochemical advantages translate into PSA detection in the 5–200 ng mL^{-1} range, with a detection limit of 5 ng mL^{-1}, accompanied by good signal stability, selectivity against common interferents, and acceptable repeatability. Preliminary *in vitro* biological interference studies further demonstrated that common serum components, including ascorbic acid, glucose, and bovine serum albumin, produced only minor changes in the electrochemical response relative to the baseline. These findings indicate that the developed MWCNTs/ZnONPs-modified platform possesses good selectivity toward PSA and may be suitable for application in complex biological matrices. Overall, these features simplify fabrication and operation, reduce reliance on expensive instrumentation, and are conducive to deployment in resource-limited settings.

However, the sensor also has limitations compared to some state-of-the-art PSA assays. The detection limit is only slightly lower than the

commonly used clinical threshold (4 ng mL^{-1}), and the linear range does not extend to the very low PSA concentrations that may be important for early recurrence monitoring but not for very early diagnosis. In addition, the present study was performed in model solutions, systematic validation in human serum or plasma, including comparison with standard ELISA measurements, is still required to fully establish analytical accuracy and robustness in complex matrices.

Data availability

The data will be made available upon request.

CRediT authorship contribution statement

Chiravoot Pechyen: Writing – original draft, Visualization, Methodology, Investigation, Formal analysis, Data curation, Conceptualization. **Khanittha Ponsanti:** Writing – review & editing, Methodology, Investigation, Formal analysis, Data curation. **Benchamaporn Tangnorawich:** Validation, Supervision, Methodology, Investigation, Data curation, Conceptualization. **Surachet Toommee:** Writing – review & editing, Resources, Methodology, Investigation. **Yardnapar Parcharoen:** Writing – review & editing, Supervision, Project administration, Methodology, Funding acquisition, Conceptualization.

Declaration of competing interest

The authors declare the following financial interests/personal relationships which may be considered as potential competing interests: Yardnapar Parcharoen reports financial support was provided by Thammasat University. If there are other authors, they declare that they have no known competing financial interests or personal relationships that could have appeared to influence the work reported in this paper.

Acknowledgements

The research team thanks the Thammasat University Research Fund for granting the -Thammasat University Research Fund (TUFT 004/2569). The research team appreciates the Graduate Development Scholarship NRCT from The National Research Council of Thailand for funding this study.

Supplementary materials

Supplementary material associated with this article can be found, in the online version, at doi:10.1016/j.bbiosy.2026.100135.

Data availability

Data will be made available on request.

References

[1] Nabok A, Abu-Ali H, Takita S, Smith DP. Electrochemical detection of prostate cancer biomarker PCA3 using specific RNA-based aptamer labelled with ferrocene. Chemosensors 2021;9:59. https://doi.org/10.3390/chemosensors9040059.
[2] Loeb S, Carter HB, Berndt SI, Ricker W, Schaeffer EM. Prostate-specific antigen testing for prostate cancer screening and management. Eur Urol 2022;82:398–412. https://doi.org/10.1016/j.eururo.2022.06.006.
[3] Liu Y, Zhang N, Pan JB, Song J, Zhao W, Chen HY, Xu JJ. Ultrasensitive electrochemical detection of biomolecules using a novel nanocomposite sensor. Anal Chem 2022;94:3005–12. https://doi.org/10.1021/acs.analchem.1c05383.
[4] Khan MS, Dighe K, Wang Z, Srivastava I, Daza E, Schwartz-Dual AS, Ghannam J, Misra SK, Pan D. Development of an amperometric immunosensor for prostate specific antigen employing advanced nanomaterials. Analyst 2018;143:1094–103. https://doi.org/10.1039/c7an01764c.
[5] Zhang Y, Li Y, Wang X, et al. Functional biomaterial interfaces for electrochemical biosensing applications. Biomater Biosyst 2023;10:100073. https://doi.org/10.1016/j.bbiosy.2023.100073.
[6] Cai G, Yu Z, Ren R, Tang D. Exciton–plasmon interaction between AuNPs/graphene nanohybrids and CdS quantum dots/TiO_2 for photoelectrochemical aptasensing of prostate-specific antigen. ACS Sens 2018;3:632–9. https://doi.org/10.1021/acssensors.7b00899.
[7] Lin Q, Yu Z, Lu L, Huang X, Wei Q, Tang D. Smartphone-based photoelectrochemical immunoassay of prostate-specific antigen based on Co-doped bi_2o_2s nanosheets. Biosens Bioelectron 2023;230:115260. https://doi.org/10.1016/j.bios.2023.115260.
[8] Zeng R, Qiu M, Wan Q, Huang Z, Liu X, Tang D, Knopp D. Smartphone-based electrochemical immunoassay for point-of-care detection of SARS-CoV-2 nucleocapsid protein. Anal Chem 2022;94:15155–61. https://doi.org/10.1021/acs.analchem.2c03606.
[9] Zeng R, Xu J, Liang T, Li M, Tang D. Photocurrent-polarity-switching photoelectrochemical biosensor for switching spatial distance electroactive tags. ACS Sens 2023;8:317–25. https://doi.org/10.1021/acssensors.2c02314.
[10] Chen S, et al. Electrochemical biosensing platform for sensitive detection of prostate-specific antigen. Biosens Bioelectron 2021;191:113461. https://doi.org/10.1016/j.bios.2021.113461.
[11] Rovina K, Siddiquee S, Shaarani SM. Cytotoxicity and biosensing implications of drug-induced toxicity: insights from electrochemical sensors. Drug Chem Toxicol 2019;42:407–14. https://doi.org/10.1080/01480545.2019.1601210.
[12] Pan Y, Zuo J, Hou Z, Huang Y, Huang C. Recent advances in electrochemical sensing platforms for biomolecules using nanomaterials. Front Chem 2020;8:592538. https://doi.org/10.3389/fchem.2020.592538.
[13] Zhang W, et al. Recent advances in electrochemical biosensors for cancer biomarker detection. TrAC Trends Anal Chem 2021;143:116382. https://doi.org/10.1016/j.trac.2021.116382.
[14] Wang J, et al. Nanomaterial-enabled electrochemical biosensors for point-of-care diagnostics. Nano Today 2020;33:100879. https://doi.org/10.1016/j.nantod.2020.100879.
[15] Yu Z, Gong H, Xu J, Li Y, Zeng Y, Liu X, Tang D. Exploiting photoelectric activities and piezoelectric properties of $NaNbO_3$ semiconductors for point-of-care immunoassay. Anal Chem 2022;94:3418–26. https://doi.org/10.1021/acs.analchem.2c00066.
[16] Yu Z, Tang Y, Cai G, Ren R, Tang D. Paper electrode-based flexible pressure sensor for point-of-care immunoassay with digital multimeter readout. Anal Chem 2019;91:1222–6. https://doi.org/10.1021/acs.analchem.8b04635.
[17] Bandeira M, Giovanela M, Roesch-Ely M, Devine DM, da S, Crespo J. Green synthesis of zinc oxide nanoparticles: a review of the synthesis methods and their antimicrobial activity. Sustain Chem Pharm 2020;15:100223. https://doi.org/10.1016/j.scp.2020.100223.
[18] Zhang L, Wang Y, Li J, et al. ZnO/MWCNT hybrid nanocomposites for ultrasensitive electrochemical detection of biomolecules. Biosens Bioelectron 2021;188:113350. https://doi.org/10.1016/j.bios.2021.113350.
[19] Nguyen TT, Tran QV, Le HT, et al. Green-synthesized ZnO nanostructures for high-performance electrochemical sensors. Microchim Acta 2022;189:226. https://doi.org/10.1007/s00604-022-05187-5.
[20] Maafa IM. Potential of zinc oxide nanostructures in biosensor application. Biosensors 2025;15(1):61. https://doi.org/10.3390/bios15010061.
[21] Maafa IM. Potential of zinc oxide nanostructures in biosensor applications. Biosensors 2025;15:61. https://doi.org/10.3390/bios15010061.
[22] Etisen AK, et al. Microfluidic and lab-on-a-chip platforms for biosensing and diagnostics. Lab Chip 2021;21:399–420. https://doi.org/10.1039/D0LC00979A.
[23] Kumar P, Singh A, Lee SH. Charge transfer dynamics in carbon nanotube–metal oxide composites for biosensor applications. Appl Surf Sci 2022;597:153708. https://doi.org/10.1016/j.apsusc.2022.153708.
[24] Chen J, Liu M, Wang Q. Conductive polymer/metal oxide nanocomposites for electrochemical biosensing applications. Biomater Adv 2023;148:213987. https://doi.org/10.1016/j.bioadv.2023.213987.
[25] Patterson AL. The Scherrer formula for X-ray particle size determination. Phys Rev 1939;56:978–82. https://doi.org/10.1103/PhysRev.56.978.
[26] Guo Q, Sun C, Li Y, Li K, Tai X. Novel poly(9-hydroxyfluorene)/NiO flower-like microspheres with good energy storage performance for supercapacitor application. Polymers 2025:128833.
[27] Zhang Y, et al. Carbon nanomaterials for electrochemical biosensing applications. Carbon N Y 2021;178:477–95. https://doi.org/10.1016/j.carbon.2021.03.042.
[28] Li X, et al. Nanomaterial-based electrochemical biosensors for sensitive biomolecule detection. Biosens Bioelectron 2022;208:114233. https://doi.org/10.1016/j.bios.2022.114233.
[29] Karim-Nezhad G, Sarkary A, Khorablou Z, Dorraji PS. Development of a voltammetric sensor based on modified carbon paste electrode for the determination of folic acid. Iran J Pharm Res 2018;17:52–62. https://doi.org/10.22037/ijpr.2018.114704.12075.
[30] Wang H, et al. Electrochemical biosensor platforms for point-of-care applications. Biosens Bioelectron 2020;165:112377. https://doi.org/10.1016/j.bios.2020.112377.
[31] Li Y, Zhang X, Wang Y, Liu S, Zhao W. Advanced nanomaterial-based electrochemical biosensors for prostate-specific antigen detection. Biosens Bioelectron 2022;197:113778. https://doi.org/10.1016/j.bios.2021.113778.
[32] Li D, Zhang Q, Zhou R, et al. Eco-friendly synthesis of ZnO nanostructures for label-free electrochemical biosensors. Electrochim Acta 2024;468:143162. https://doi.org/10.1016/j.electacta.2023.143162.
[33] Jeyachandran YL, Mielczarski JA, Mielczarski E, Rai B. Efficiency of blocking of non-specific interaction of different proteins by BSA adsorbed on hydrophobic and hydrophilic surfaces. J Colloid Interface Sci 2010;341:136–42.
[34] Wilkirson EC, Singampalli KL, Li J, Dixit DD, Jiang X, Gonzalez DH, Lillehoj PB. Affinity-based electrochemical sensors for biomolecular detection in whole blood. Anal Bioanal Chem 2023;415:3983–4002.

[35] Powers JL, Rippe KD, Imarhia K, Swift A, Scholten M, Islam N. Integrating green chemistry into analytical chemistry education through project-based learning. J Chem Educ 2021;89:1587–90. https://doi.org/10.1021/acs.jchemed.1c00227.
[36] Assari P, Rafati AA, Feizollahi A, Asadpour Joghani R. An electrochemical immunosensor for the prostate specific antigen based on reduced graphene oxide decorated with gold nanoparticles. Microchim Acta 2019;186:484. https://doi.org/10.1007/s00604-019-3565-8.
[37] Chen ZA, Lu W, Bao C, Niu Q, Cao X, Wang H, Yao RX. Copper(II) 1,4-naphthalenedicarboxylate on copper foam nanowire arrays for electrochemical immunosensing of the prostate specific antigen. Microchim Acta 2019;186:758. https://doi.org/10.1007/s00604-019-3891-x.
[38] Feng J, Wang H, Ma Z. Ultrasensitive amperometric immunosensor for the prostate specific antigen by exploiting a Fenton reaction induced by a metal–organic framework nanocomposite of type Au/Fe-MOF with peroxidase-mimicking activity. Microchim Acta 2020;187:95. https://doi.org/10.1007/s00604-019-4075-4.
[39] Wei B, Mao K, Liu N, Zhang M, Yang Z. Graphene nanocomposites modified electrochemical aptamer sensor for rapid and highly sensitive detection of prostate specific antigen. Biosens Bioelectron 2018;121:41–6. https://doi.org/10.1016/j.bios.2018.08.067.
[40] Farzin L, Sadjadi S, Shamsipur M, Sheibani S. An immunosensing device based on inhibition of mediator's faradaic process for early diagnosis of prostate cancer using bifunctional nanoplatform reinforced by carbon nanotube. J Pharm Biomed Anal 2019;172:259–67. https://doi.org/10.1016/j.jpba.2019.05.008.
[41] Zhu L, Lv Z, Yin Z, Li M, Tang D. Digital multimeter-based point-of-care immunoassay of prostate-specific antigen coupling with a flexible photosensitive pressure sensor. Sens Actuators B Chem 2021;343:130121. https://doi.org/10.1016/j.snb.2021.130121.
[42] Yu Z, Zeng R, Qiu M, Tang D, Knopp D. $NaNbO_3$-based piezo-phototronic immunosensing platform for point-of-care testing. Biosens Bioelectron 2022;197:113778. https://doi.org/10.1016/j.bios.2021.113778.